Aerospace Science and Technology 89 (2019) 1–10

Contents lists available at ScienceDirect

Aerospace Science and Technology

www.elsevier.com/locate/aescte

Open and closed loop gust loads analyses for a flying wing configuration with variable longitudinal stability

A. Voß

DLR (German Aerospace Center), 37073 Göttingen, Germany

ARTICLE INFO

Article history:
Received 25 January 2019
Received in revised form 7 March 2019
Accepted 7 March 2019
Available online 1 April 2019

Keywords:
Flying wing
Gust loads
Closed loop
Structural optimization

ABSTRACT

This work presents results of dynamic "one-minus-cosine" gust load simulations for a flying wing configuration. The in-house toolbox Loads Kernel is used for the loads analysis of the free flying aircraft. Flight mechanical characteristics are captured by application of a non-linear equation of motion in the time domain. The underlying aerodynamic methods are the Vortex Lattice and the Doublet Lattice Method with a rational function approximation (RFA) for unsteady simulations in the time domain. The structural model was created using DLR's parametric ModGen/Nastran design process. The structure is optimized for minimum structural weight with typical design load cases including maneuver, gust and landing loads. In this article, the focus lies on gust encounters and the flight characteristics of a flying wing configuration. It differs from classical configurations (wing-fuselage-empennage) due to a pronounced nose-up pitching motion when the aircraft enters the gust field. Finally, a flight controller is designed to increase the pitching stability. This is essential for the flight of a naturally unstable configuration. It is shown that the loads during a gust encounter increase significantly. The influence on the structural weight is small as the layout is very robust and the required material thickness is below the minimum thickness in most areas.

1. Introduction

The multidisciplinary configuration MULDICON is a flying wing configuration with wings of low aspect ratio. The geometry is used for a wide range of activities such as numerical aerodynamics or wind tunnel investigations. Real-sized design concepts are developed by Liersch et al. [1,2] and Krüger et al. [3] Aeroelastic models are developed by Voß and Klimmek [4] and Bramsiepe et al. [5]. These models have been used by Schäfer et al. [6] for body freedom flutter analyses and by Voß and Klimmek [7] for maneuver loads analysis using computational fluid dynamics (CFD) corrected potential methods. In addition, the MULDICON is investigated internationally within the NATO STO AVT-251 working group as presented by Cummings et al. [8] and Schweiger at al. [9]. An overview on further, geometrically similar configurations is found in previous work [7,4,5].

The pitching stability of an aircraft is determined by the location in longitudinal direction of the center of gravity (CG) in combination with the center of pressure (CP). A CG in front of CP results in a stable aircraft. This is the case for most aircraft and mandatory for all civil aircraft. Typically, there is a movement of CG due to passengers, payload or fuel tank levels while the shift of CP is small. To maintain a certain longitudinal stability, the horizontal tail is used. The same holds for flying wings, except that they are very sensitive to any movement of CP and CG. There is no stabilizing tail and the control surfaces are typically located along the trailing edge and have short lever arms. Therefore, flying wings are expected to be very sensitive to an external disturbance, such as gust encounter. This leads to the following objectives for this work:

- Extend the simulation capabilities of gust encounter to include rigid body motion and penetration effects already in the preliminary design.
- Assess the impact of a gust encounter on the MULDICON with respect to flight mechanics and loads.
- Re-evaluate and quantify the resulting loads in terms of section loads and structural weight for a gust encounter with an active flight controller to increase pitching stability.

The work is an extension of [10] and is structured as follows: The set-up of the stiffness and mass models is presented in section 2. In section 3, the theoretical background of the time simulation is described shortly. In section 4, the MULDICON is exposed to a series of gust encounters and the corresponding loads are evaluated.

E-mail address: arne.voss@dlr.de.

https://doi.org/10.1016/j.ast.2019.03.049

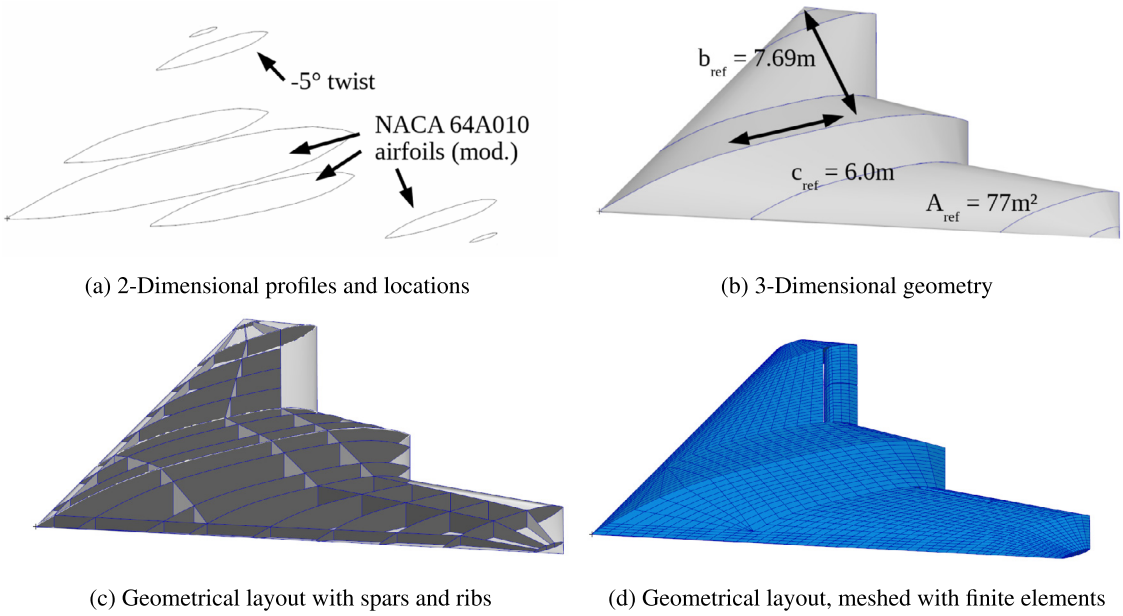

(a) 2-Dimensional profiles and locations

(b) 3-Dimensional geometry

(c) Geometrical layout with spars and ribs

(d) Geometrical layout, meshed with finite elements

Fig. 1. From 2-Dimensional model information to FE model.

The layout and set-up of a simple flight controller for the pitching motion is presented in section 5.1. Sections 5.2 and 5.3 show the influence of the controller in terms of section loads, first of the natural stable, than of the unstable configuration. A structural optimization follows in 5.4. Finally, a conclusion and an outlook on future work is given in section 6.

2. Weight optimized structural and mass models

The aeroelastic models of the MULDICON were built and optimized for structural weight in a previous work by Bramsiepe, Voß and Klimmek [4,5,11]. The structural and mass models are set-up using a parametric design process. Starting with general information of the aircraft layout, a parametric geometry model is generated using the in-house software ModGen [12]. For the MULDICON, the profiles and the planform is already given. From that information, three dimensional segments are constructed, one between each of the profiles, as shown in Fig. 1a and Fig. 1b. The positions of spars and ribs are defined, resulting in Fig. 1c. That geometrical layout is meshed using finite elements, resulting in Fig. 1d. In the case of the MULDICON, mainly shell elements are used. Beam elements are added as stiffening elements for the spars and ribs. For the upper and lower skin, stringers with hat profiles support the shell elements. Fig. 2 shows the inner layout with sufficient space for the engine (red), the payload bay (yellow) as well as the nose and main landing gear bays (green).

The material of the shell elements is carbon fiber reinforced plastic (CFRP). Several layers of unidirectional (UD) fibers are combined to a laminate. The behavior of the laminate can be tracked back to the properties of the individual layers. The calculation principles are based on the classical laminate theory (CLT). A very useful summary of the state of the art and practical advice on the development and analysis of CFRP components is published by the Verein Deutscher Ingenieure in guideline VDI 2014, Part 3 [13], available in German and English.

The engine mass is derived from a related design task by Becker et al. [14] and Nauroz [15] within the Mephisto project. Masses for the landing gears are estimated using an in-house software. The fuel tanks are modeled geometrically using ModGen and filled to a required level. With this procedure, the mass, inertia and center of gravity for each section between two ribs and spars is analyzed

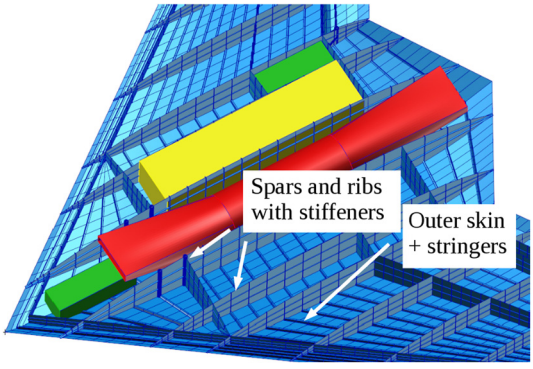

Fig. 2. Inner, structural layout and FE modeling with spaces for engine (red), payload (yellow) and landing gears (green). (For interpretation of the colors in the figure(s), the reader is referred to the web version of this article.)

numerically. For additional systems, masses are estimated. The corresponding mass discretization is shown in Fig. 3. Nine different mass configurations ranging from 5.9t (no fuel, no payload) to 13.1t (full fuel, full payload) are used to reflect different phases of flight during the mission. The dynamic analysis of the stiffness and mass model should result in almost only global modes for a specified frequency range. Local modes are to be avoided. Because the configuration is rather stiff, only the first 10-19 modes will be considered in this study. The selected number of modes is determined for every mass configurations individually, as the eigenfrequencies change significantly with the mass configuration.

In a next step, the structural model is subject to an optimization using MSC.Nastran SOL200. The design objective is minimum structural weight. The design variable is the skin thickness of every design field, with one design field being the area between two ribs and spars, while the topology of the structural layout, see Fig. 1 and 2, remains unchanged. During the optimization process of the structural model, a total of 306 maneuver load cases as well as 336 gust load cases are taken into account. In addition, a new, simplified landing impact simulation [5] is introduced to consider 12 landing load cases. Such a fairly high number of load cases is necessary to cover a sufficient number of flight conditions as well as to take into account that different parts of the aircraft are sized by different design load cases.

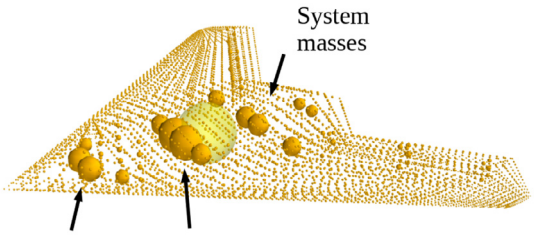

(a) Structure and system masses

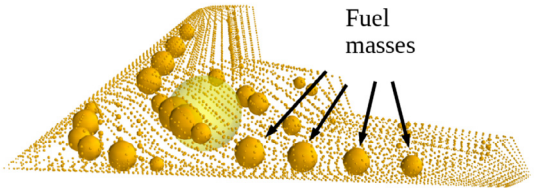

(b) Structure, system masses and fuel masses

Fig. 3. Two exemplary mass configurations of the MULDICON.

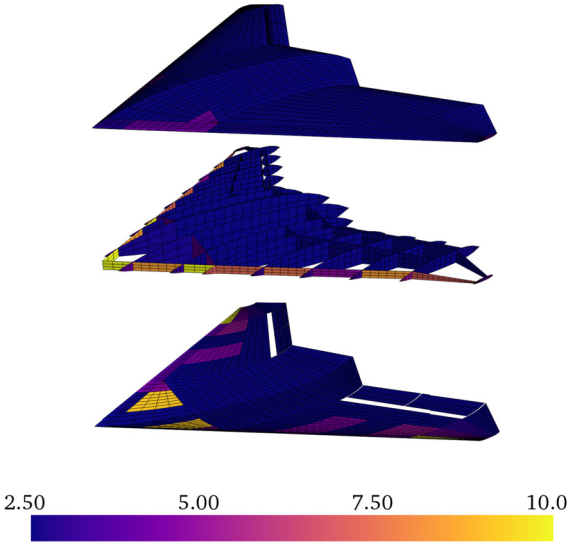

Fig. 4. Resulting material thickness distribution after optimization in [mm].

The optimization is an iterative procedure. After three outer loops of loads calculation followed by an optimization, convergence is achieved. The resulting model has a structural net weight of 1511 kg and a material thickness distribution as shown in Fig. 4. Although the dimensioning criterion is selected conservatively, the material thickness is in most areas the minimum thickness of 2.5 mm and only some regions along the leading edge and at the wing tip are reinforced. This can be explained by the geometrical shape, which is rather thick in the center region to accommodate the engine and to provide space for payload, fuel and other aircraft systems. At the same time, the wing is very short and thus produces comparatively low bending moments. Removing some structural members could result in an even lighter design. However, most spars and ribs are required for the attachment of aircraft systems or serve as fuel bays. Ribs are also required to maintain the shape of the airfoil. Although payload and landing gear bays are planned, the outer skin is closed in the structural model. Additional cutouts for payload and landing gear doors might weaken the structure, leading to a different result. Investigations on this topic are ongoing and not subject of this article.

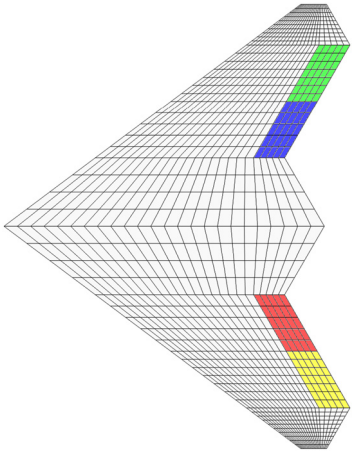

Fig. 5. Aerodynamic panel mesh of the MULDICON.

3. Theoretical methods

The classical aerodynamic approach with the steady Vortex Lattice Method (VLM) and the unsteady Doublet Lattice Method (DLM) is chosen. The formulation of the VLM follows closely the derivation given by Katz and Plotkin [16] using horse shoe vortices. The DLM is formulated as given by Albano and Rodden [17]. The VLM and the DLM are based on a matrix of aerodynamic influence coefficients (AIC), which depends on the Mach number Ma, the reduced frequency $k = \frac{\pi \cdot F \cdot c_{ref}}{U_\infty}$ and the geometry of the aircraft. In general, the discretization of such a highly swept geometry needs to be a compromise between the long wing root and the short wing tip. Jumps in the discretization are to be avoided. The resulting mesh is shown in Fig. 5 and has 1248 panels. It includes four control surfaces along the trailing edge, which are highlighted in the top view in Fig. 5. In general, both VLM and DLM are limited to the subsonic regime, but may be corrected to include transonic effects such as compression shocks. For simplicity, in this work, the AIC matrices are not corrected, as such a correction would mainly effect the initial horizontal flight condition. The assumption is that a gust encounter is dominated by unsteady aerodynamics, structural dynamics, rigid body motion and the interaction with a flight controller.

In this work, unsteady aerodynamic forces in the time domain are obtained by a rational function approximation (RFA) as suggested by Roger [18]. The time domain is preferred over the frequency domain as it allows non-linearities for example in the rigid body motion and in the closed-loop system.

Other authors, for example Karpel et al. [19] and Teufel and Kruse [20], perform a coupling of linear calculations in the frequency domain with selected non-linear parts in the time domain, aiming for a higher efficiency in terms of calculation time. In addition, the approximation of the unsteady aerodynamic forces is avoided but a more complex mathematical procedure is introduced including several transformations from frequency into time domain and vice versa. The equation of motion is linear in the frequency domain and problems might arise for naturally unstable configurations. Therefore, the time domain approach is more general and the preferred solution in this work.

The gust velocity U is defined by the certification specifications CS 25.341 [21] in dependence of the distance s penetrated into the gust and the design gust velocity U_{ds}. The so-called gust gradient H determines the length (parallel to the aircraft's flight path) for the gust to reach its peak velocity.

$$U = \frac{U_{ds}}{2}\left[1 - cos\left(\frac{\pi s}{H}\right)\right] \quad for \quad 0 \le s \le 2H \tag{1}$$

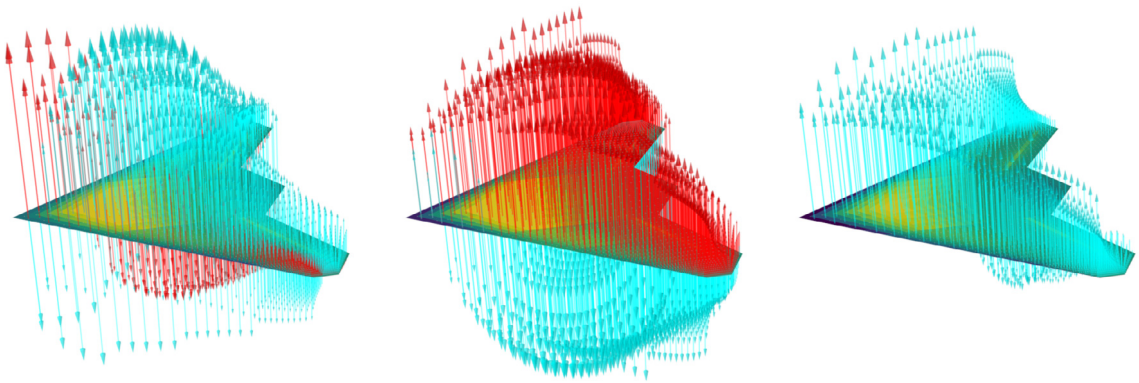

(a) t=0.03s (b) t=0.07s (c) t=0.11s

Fig. 6. Temporal evolution of aerodynamic gust forces (red) and unsteady forces (cyan).

The gust encounter is always considered on top of the horizontal level flight. Therefore, the quasi-steady trimmed state of the horizontal level flight is calculated first and taken as initial condition for the time domain simulation of the gust encounter.

The equation of motion is split in two parts. A non-linear part for the rigid body motion is derived from Waszak, Schmidt and Buttrill [22–24]. Structural flexibility is incorporated using a second, linear elastic equation on motion on a modal basis.

For more details on the theoretical background and the corresponding equations, please consult sections 3, 4 and 5 in [10].

4. Physical effects during a gust encounter, open loop

In general, the MULDICON has a very distinct, physical behavior during an gust encounter, deviating from classical configurations. One effect is the penetration into the gust field, visualized in Fig. 6. The aerodynamic force vectors due to the gust are shown in red color and the unsteady aerodynamic contributions are shown in cyan color. Note that the magnitude of the vectors is scaled non-linearly to highlight small forces. The qualitative meaning is enhanced while the quantitative meaning is lost. The selected gust is the shortest according to certification specifications, has a gradient (total length = 18 m) and has a positive orientation (gust from below/upgust). In Fig. 6a, the gust has just reached the aircraft nose, resulting in the gust forces (red) to point upwards. The additional lift at the nose immediately induces velocities on the other areas of the aircraft, for example on the rear fuselage and the wing tips. The delay in time is not captured. Due to the sudden change in downwash, unsteady aerodynamic forces (cyan) occur, counteracting the impact of the gust and thus introducing the lagging behavior. In Fig. 6b, the aircraft is approximately in the center of the gust field. The gust shape is clearly visible when looking at the gust force vectors (red). In Fig. 6c, the aircraft has just left the gust field and there are no more aerodynamic gust forces (red). However, the gust has still an indirect aerodynamic impact on the aircraft as the unsteady aerodynamic forces (cyan) still exist. In contrast to the middle picture, they point upwards. Their magnitude will decrease quickly within the next time steps. Note that in this implementation, unsteady effects are also calculated for flexible and rigid body motion. As the aircraft is still in motion, some unsteady forces will remain.

This physical behavior is also reflected in the section loads. Here, a quantitative assessment is possible. Fig. 7 shows the contributions of different forces to the shear force F_z at the wing root. With the green dashed line the quasi-steady and with red triangles the unsteady aerodynamics are plotted. As expected from Fig. 6, the unsteady aerodynamic forces first act in the same direction

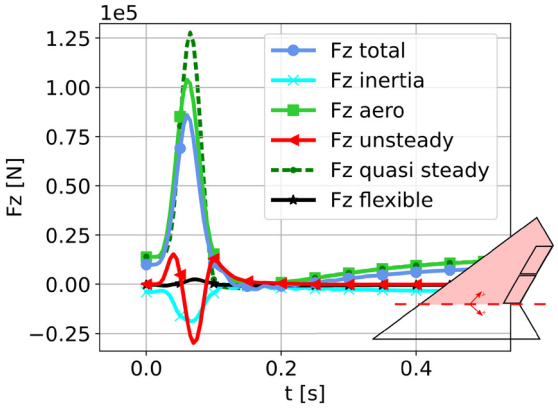

Fig. 7. Composition of the right wing root shear force F_z in detail.

as the quasi-steady aerodynamics (positive sign) and then start to counteract (negative sign) and have a peak at 0.7 s when the aircraft is completely immersed in the gust field, compare with Fig. 6. Therefore, they not only reduce the peak of the quasi-steady aerodynamics but also cause the peak to occur more early in time. The sum of both lead to the aerodynamic forces plotted with green squares. The inertia force is plotted with cyan crosses. The sum of both leads to the total force, plotted with blue dots. Finally, the aerodynamic force due to structural flexibility are plotted with black stars. One can see that they only have a minor contribution.

Another physically interesting effect is the rigid body motion of the aircraft in the gust field. The MULDICON is designed with only a small stability margin of 3.0%MAC. Therefore, the center of pressure is close to the center of gravity. In a gust encounter, this normally results in a comparatively large heave motion and only a small pitching motion because the pitching moment about CG is small. However, due to the lack of an empennage, the MULDICON is very sensitive to the pitching motion. In addition, a large share of the aerodynamic surface is in front of CG. The flight characteristics are studied more closely by examining the pitch angle Θ and the pitch rate q. Fig. 8 shows the results for a selected number of positive gust encounters (gust from below/upgust) of one exemplary mass configuration and gust gradients ranging from $H = 9m$ to $107m$. In all cases, the aircraft experiences a positive, nose up pitching motion. This is contrary to the behavior observed with classical configurations which typically dive into the gust (nose down) and presumably increases the aircraft loads.

A quantification of the loads due to the pitching motion is achieved by comparing a free-free gust encounter with a gust encounter with suppressed pitching motion. The results for the shear

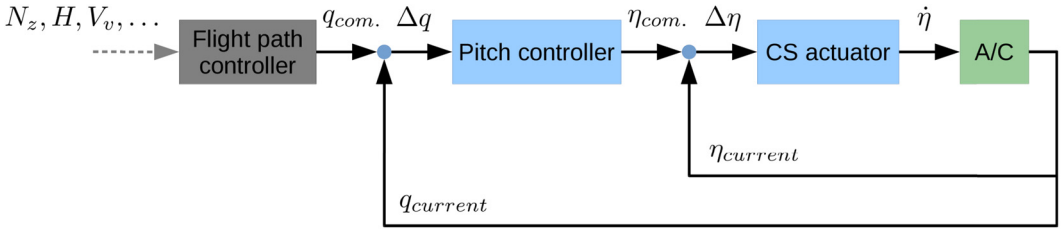

Fig. 10. Layout of a flight controller for pitching motion.

force F_z, bending moment M_x and torsion moment M_y at the right wing root are shown in Fig. 9. The difference between the free-free and supported loads in blue and green can be attributed to the pitching motion.

5. Physical effects during a gust encounter, closed loop

5.1. Active pitch control

The flight controller for the MULDICON considered in this work is restricted to the control of the pitching motion only. The aim is to maintain a commanded pitch rate q_{com} even when the aircraft is subject to external disturbances such a gust encounter. The proposed flight controller is shown in Fig. 10 and consists of two cascaded feedback loops. The commanded pitch rate q_{com} may stem from the pilot's stick command or a flight path control system shown in gray color. For simplicity, the commanded pitch rate q_{com} is assumed to be given. The pitch controller consists of a proportional and an integral control element with coefficients K_p and K_i. If a more aggressive behavior is desired, a differentiating element with coefficient K_d may be added. The output of the pitch controller is the commanded control surface deflection η_{com}. The control surface actuator consists of a proportional element and returns the control surface rate $\dot{\eta}$. The MULDICON has four control surfaces, as described in section 3. For pitch control, all four control surfaces are desired to behave identically, requiring only one actuator model in the simulation. The actuator has a proportional coefficient K_p and becomes non-linear by enforcing a maximal actuator rate $\dot{\eta} = \pm 40°/s$ to reflect the abilities of a typical hydraulic actuation system. The two control loops of the pitch controller and the actuator are closed by the feedback of the actual pitch rate q_{current} and the actual control surface deflection η_{current} of the aircraft. Note that a load reduction is not the driving factor for the selection of the control coefficients. The values of the coefficients K_p and K_i are determined in a simple, iterative procedure to minimize the Integral of Absolute Error Criterion A_{IAE}, which describes the difference between commanded signal q_{com} and system reaction q.

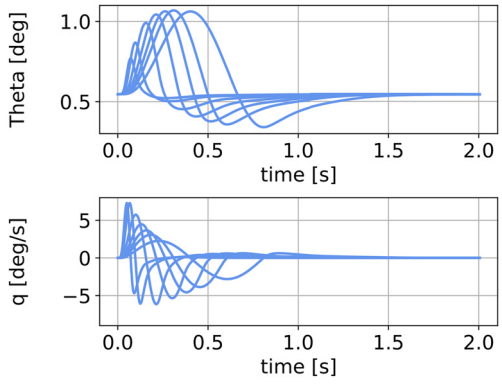

Fig. 8. Pitch angle Θ and pitch rate p for selected gust encounters.

5.2. Naturally stable configurations

The MULDICON is exposed to a series of gust encounters again, this time with the flight control system switched on. The flight control system presented in the previous section has been implemented in the flight loads environment. The dashed lines in Fig. 11 show the pitch angle Θ and the pitch rate q of the uncontrolled aircraft. Again, encounters of a positive gust (gust from below/upgust) of one exemplary mass configurations and gust gradients ranging from $H = 9m$ to $107m$ are shown. The blue lines show the results of the closed loop system. Comparing the open and closed loop system, the maximum pitch angle is reduced by approximately 60% and the minimum pitch angle is reduced by approximately 30% with respect to the initial value. For the open loop system, the minimum and maximum values are reached by the longer gusts while in the closed loop system, the minimum and maximum values are caused by the short gusts. In addition, the short gusts show a more pronounced overshoot, which is also reflected in the pitch rate q. Summing up, it is observed the controller of the closed loop system performs excellently with some troubles with the shorter gusts. This behavior is as expected and

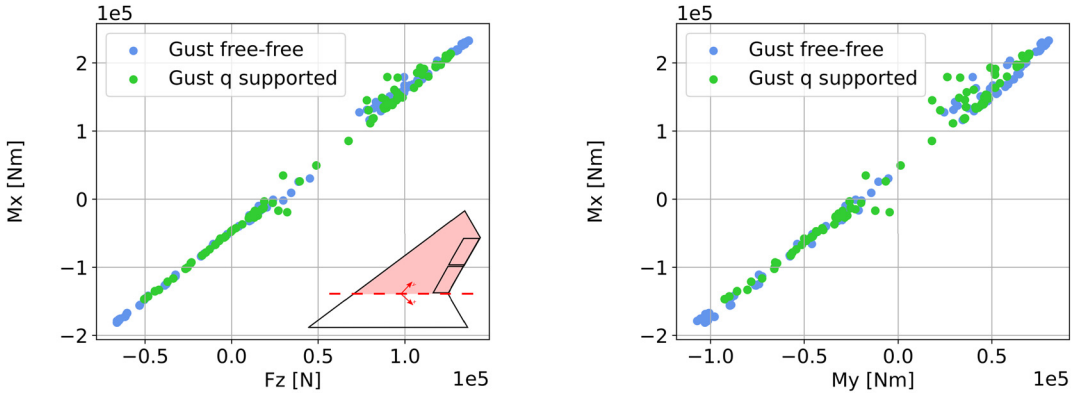

Fig. 9. Loads envelope of shear force F_z, bending moment M_x and torsion moment M_y at the right wing root.

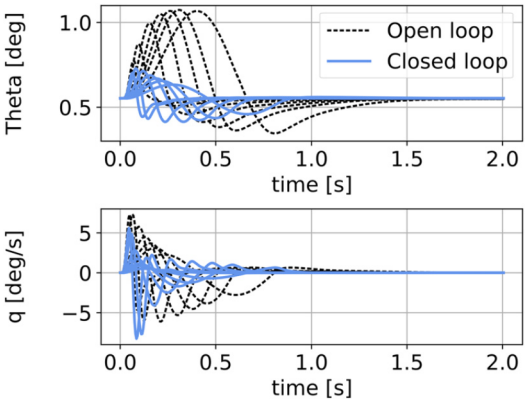

Fig. 11. Pitch angle Θ and pitch rate q for the closed loop system.

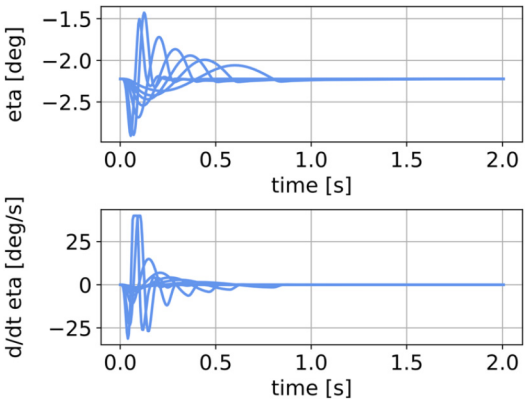

Fig. 12. Commanded control surface deflection η and control surface rate $\dot{\eta}$.

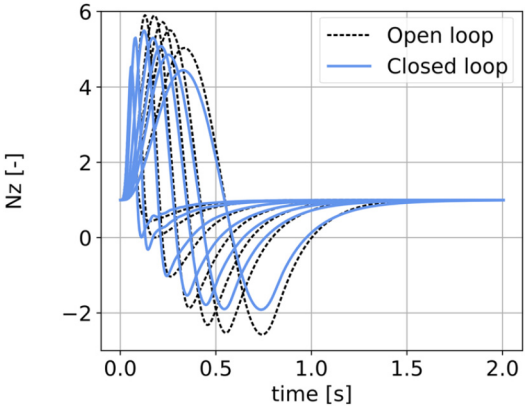

Fig. 13. Load factor N_z for the closed loop system.

caused by physical limitations such as the control surface rate $\dot{\eta}$. Fig. 12 shows the control surface deflection η and the control surface rate $\dot{\eta}$. Although only small deflections are required, the control surface is moved at high rates, hitting the limit of $\pm 40° s^{-1}$ in several cases. The performance for short gusts can only be improved with higher rates, as discussed before, or by adding prior knowledge of the gust. For classical wing-fuselage-empennage configurations, such information could be obtained by a sensor at the aircraft nose. For flying wings such as the MULDICON, a future alternative could be LIDAR techniques, measuring the flow field several meters in front of the aircraft, see for example Wang et al. [25].

To obtain a first glance on the effect on loads, the load factor N_z shown in Fig. 13 can be consulted. Because the positive, nose up pitching motion is reduced in the closed loop system, the load factor N_z is reduced as well, suggesting a reduction in loads.

In Fig. 14, the loads envelopes of shear force F_z, bending moment M_x and torsion moment M_y are shown for the right wing root. In contrast to maneuver loads, gust loads are the result of a time simulation. Therefore, the approach selected in this work involves an extraction of several snapshots from the time simulation. In this way, dynamic loads are transferred into quasi-static loads and are usable for a dimensioning process. The snapshots are selected by identifying the minimum and maximum values at every monitoring station for every interesting quantity. Every dot in Fig. 14 corresponds to one snapshot, which has been identified from the time simulation, and out of 336 gust simulations, every gust simulation produces several dots. For reference, the gust loads of the open loop simulation are shown as well. It can be seen that while the controller reduced the load factor N_z, this is not generally the case for the section loads. The envelopes of shear force F_z and bending moment M_x have a similar shape with the closed loop system leading to a slightly lower shear forces F_z and slightly higher bending moments M_x. The envelopes of bending moment M_x and torsion moment M_y of the closed loop system appear larger. In Fig. 15 the control surface attachment loads in terms of shear force F_z and torsion moment M_y are shown for the inner and outer control surface. Obviously, the actuator of the closed loop system causes much higher loads compared to the open loop system, which is as expected.

5.3. Naturally unstable configurations

The MULDICON has been designed with a positive longitudinal stability and a desired center of gravity approximately at $CG_x \approx -3.0[\%MAC]$ with the exact value depending on the mass configuration. In this section, that design restriction will be lifted and a rearward shift of CG_x will be allowed, resulting in a naturally unstable configuration. The influence on gust loads is expected to be high as the demand on the flight controller is even higher than in the previous section: no disturbances and gusts are possible for naturally unstable configurations without control.

A naturally unstable configuration might occur due to several reasons. The fuel tanks could be drained unbalanced, either on purpose or due to a system failure, resulting in a shift of CG. The payload of 2×1000 kg is assumed to be in the center of the payload bays. This is probably true for a payload of uniform shape and density. To create an unstable configuration, the payload is shifted from its design position at $x = 5.9m$ slightly rearwards to $x = 7.0m$ as indicated in Fig. 16. The payload is still located within the bounds of the payload bay and the location of CG is changed from -2.9 to $+2.4[\%MAC]$, where a positive value indicates an unstable configuration, because the CG if aft of the aerodynamic center.

In a first step, the rigid body motion is re-evaluated for the naturally unstable closed loop configuration and compared to the naturally stable closed loop configuration. Note that the closure of the naturally unstable system actually leads to a stable system. Fig. 17 shows the pitch angle Θ and pitch rate q. It can be seen that the controller performs reasonably well for short gusts but worse for longer gusts. The maximum pitch angle Θ is approximately $+1.1°$ and comparable to the results for the open loop system, see the dashed line in Fig. 11. The dynamic overshoot is much larger, leading to a minimum pitch angle Θ of about $-0.05°$. The long gusts are more difficult to control than the short gusts. This is also reflected in the pitch rates q. Still, the proposed controller of the closed loop system manages to maintain stability and leads the aircraft safely back into a horizontal flight condition. Note that there is a small offset between the naturally stable and unstable configuration already at $t = 0.0s$. This can be explained by the

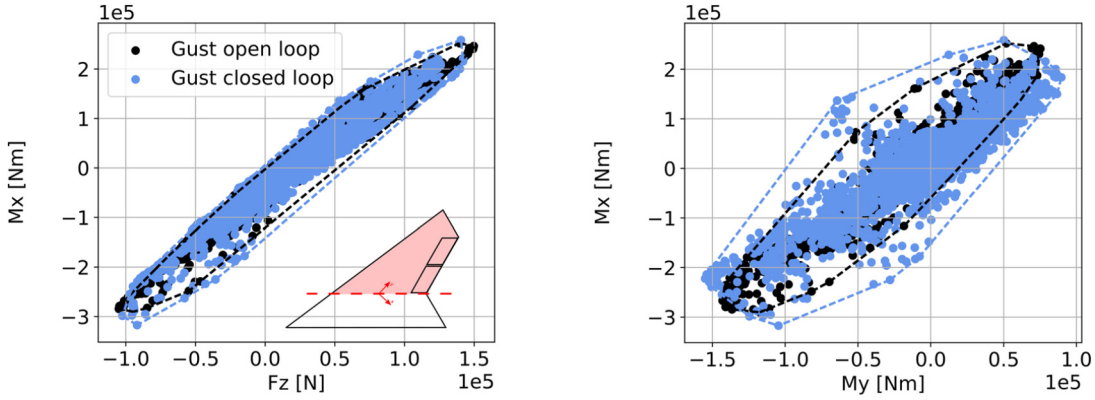

Fig. 14. Loads envelope of shear force F_z, bending moment M_x and torsion moment M_y at the right wing root.

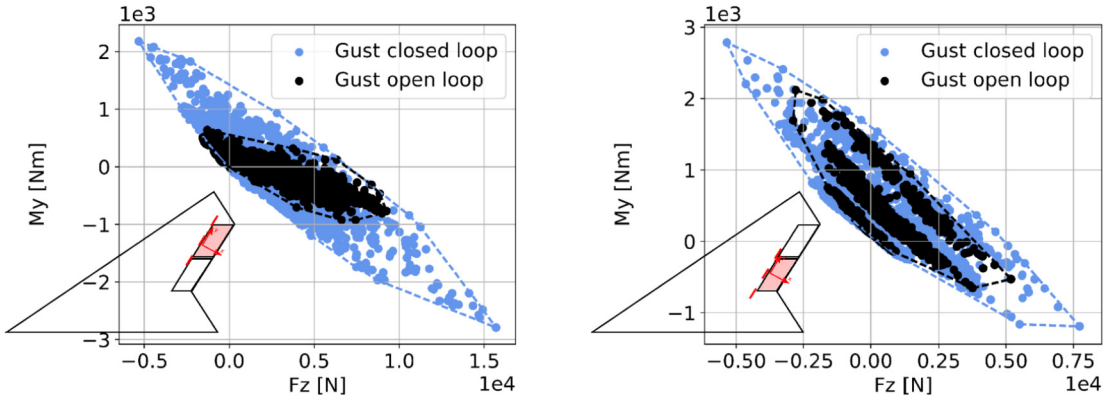

Fig. 15. Envelope of control surface attachment loads.

Fig. 16. A rearward shift of payload creates a unstable configuration. Left: stable, Right: unstable.

initial trim condition. Due to the modified mass configuration, the control surfaces are employed to balance the aircraft, leading to a new pitch angle Θ.

From Fig. 18 it can be seen that for the short gusts, the allowable control surface rate $\dot{\eta}$ is again the limiting factor. The longer gusts require larger control surface deflections η compared to the naturally stable configuration but a rate $\dot{\eta} \leq \pm 40°$ is sufficient.

The maximum load factors N_z are approximately $+6.6$ and -3.6. With the horizontal flight condition $N_z = 1.0$ as reference, this is an increase by 22% and 58% respectively compared to the naturally stable closed loop configuration (see Fig. 19).

In Fig. 20, the loads envelopes of shear force F_z, bending moment M_x and torsion moment M_y are shown for the right wing root. The envelope of shear force F_z and the bending moment M_x is significantly larger compared to the naturally stable configuration but the increase is not as large as for the load factor N_z. Surprisingly, the torsional moments M_y has the same minimum and maximum amplitude compared to the naturally stable closed loop configuration. Due to the combination with the bending moment M_x, the envelope is still larger. In the previous section, the increase of torsional moment M_y could be traced back to the control surface attachment loads, adding higher forces and moments along the trailing edge compared to the open loop system. In the case of the naturally unstable system, it can be concluded that the control surface attachment loads have approximately the same amplitudes as for the naturally stable system, leading to a similar torsional moments M_y along the wing. As discussed before, the flight controller is limited by the maximal allowable control surface rate $\dot{\eta}$ and that limit is touched for the shorter gusts with $H = 9m$ and $15m$ for both the naturally stable and unstable configuration. Therefore, the control surfaces move in a similar manner and experience a similar loading.

5.4. Influence in terms of structural weight and loading

From these observations, the next step is a reassessment of the structural optimization for minimum structural weight, including gust loads of the closed loop systems. The convergence behavior is good as shown in Fig. 21. Three outer loops lead to converged results in all cases. The use of three loops also has a physical meaning which can be interpreted as follows. The first loop gives a first estimate. If necessary, the second loop adjusts the estimate slightly and the third loop confirms the results. For the MULDICON, the first estimate is confirmed twice. The convergence can be considered as very trustable if no general trend is visible.

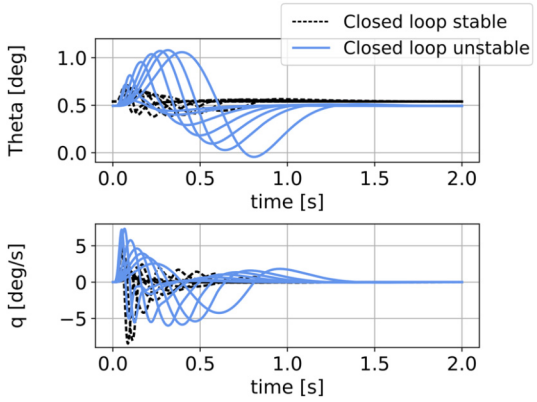

Fig. 17. Pitch angle Θ and pitch rate q for the naturally unstable system.

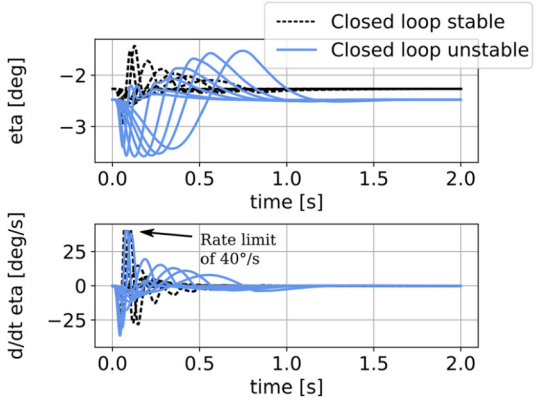

Fig. 18. Commanded control surface deflection η and control surface rate $\dot{\eta}$.

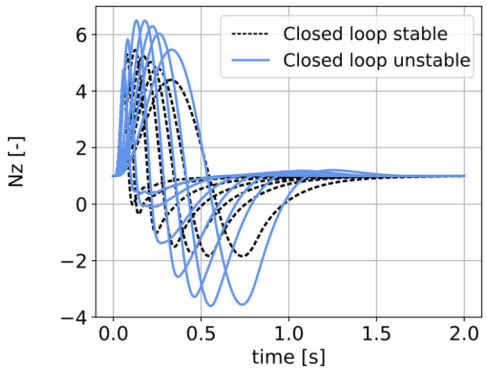

Fig. 19. Load factor N_z for the naturally unstable system.

In all cases, the final structural weight is approximately 1500 kg. The difference of approximately 20 kg is well within the precision of the optimization. Reasons for this could be the extremely high stiffness of the structure and high strength capacity. For a stress engineer, this is a very preferable situation. Although Fig. 15 showed higher control surface attachment loads, no increase of material thickness of the rear spar, where the control surfaces are attached, is observed. An inspection of the failure index of the carbon fiber material, see Fig. 22, shows that the rear spar experiences a loading higher than for example the middle spar. The magnitude is well below 1.0 so that the minimum material thickness is still sufficient.

During later phases of the aircraft design, for example during the detail design, the global structural stiffness might be reduced by holes and cut-outs in the outer skin. These might lead to different results. Also, a more detailed attachment of large non-structural system masses, such as the engine, might influence the structural characteristics, mode shapes and frequencies of the aircraft and change its global stiffness.

The optimization results are very similar and mainly the leading edge and the front spar are affected, as can be seen from the material thickness distributions plotted in Fig. 23. Apparently, a modification of these design fields has the largest impact on the overall design objective of minimum weight. This can be explained by the nature of the flight controller to steer the aircraft into the gust. This increases the effective angle of attack, resulting in a higher lift, which acts on the aircraft just behind the front spar (approximately at a local chord length of 25%). To further improve the structural layout in terms of geometry, the front spar could be shifted rearwards, which would increase its height and second area moment.

In general, it can be concluded that such a compact flying wing configuration of low aspect ratio is sized mainly by local loads.

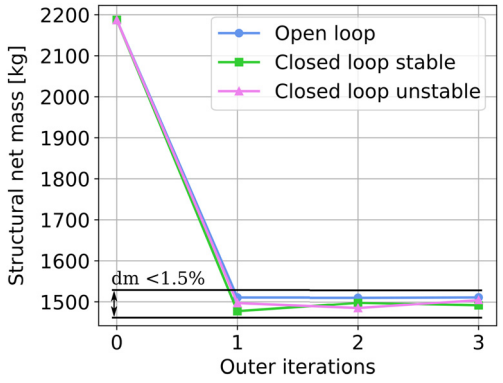

Fig. 21. Convergence history of structural net mass.

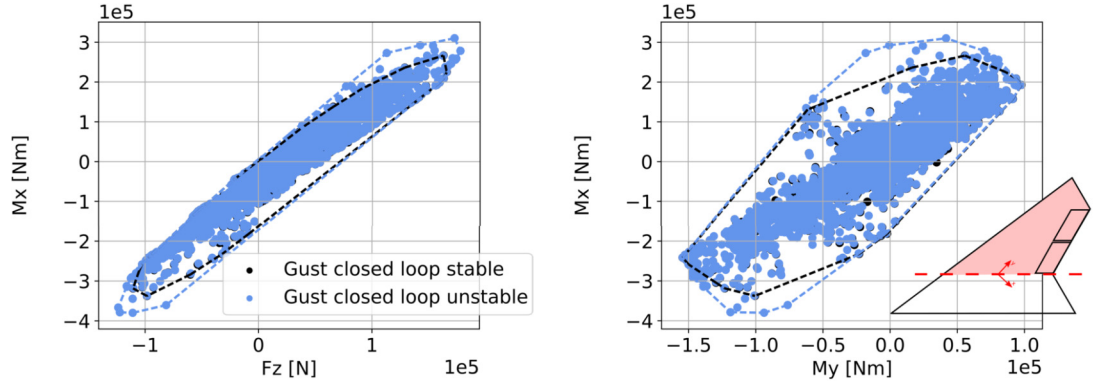

Fig. 20. Loads envelope of shear force F_z, bending moment M_x and torsion moment M_y at the right wing root.

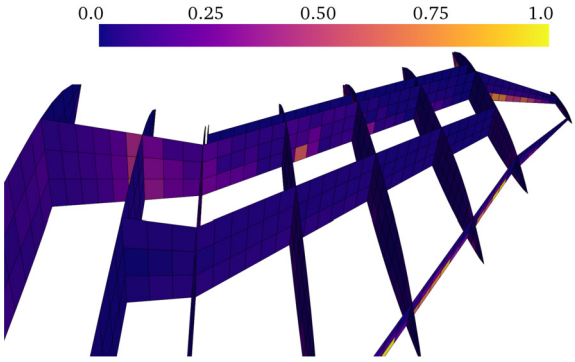

Fig. 22. Failure index of rear spar over all plies and load cases.

This is contrary to the experience with high aspect ratio wing-fuselage-empennage configurations, where the structural sizing is dominated for example by large bending moments at the wing root.

6. Conclusion and outlook

In this work, the results of dynamic 1-cos gust loads for the MULDICON are presented. The structural model of the MULDICON was created in a previous work using DLR's parametric ModGen/Nastran design process. The structure is optimized for minimum structural weight with typical design load cases including maneuver, gust and landing loads. The in-house toolbox Loads Kernel is extended in such a way to allow for dynamic, unsteady simulations in the time domain including flight mechanics of the free-flying aircraft. With this basis, physical effects are investigated that occur during a gust encounter.

The MULDICON has a strong penetration effect due to its compact, non-slender and highly swept geometry. This causes the unsteady aerodynamics to behave differently than with classical configurations. The MULDICON also shows a pronounced tendency to pitch up when entering a gust field. It can be shown that the use of the Pratt formula for quasi-steady gust loads is unsuitable.

In a next step, the MULDICON is exposed to a series of gust encounters with flight control switched on. The pitching stability is

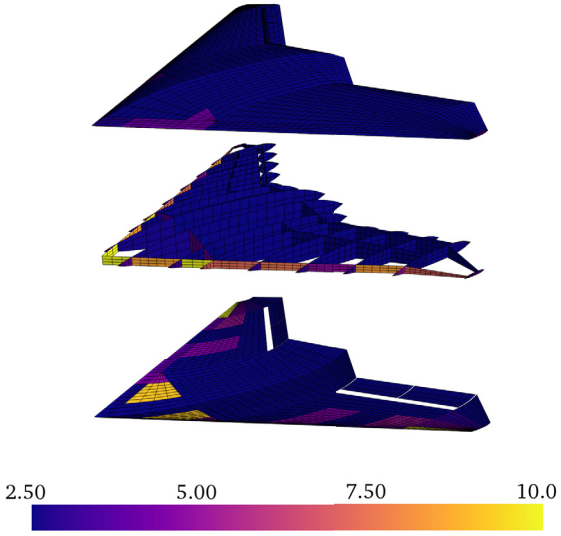

(a) Open loop

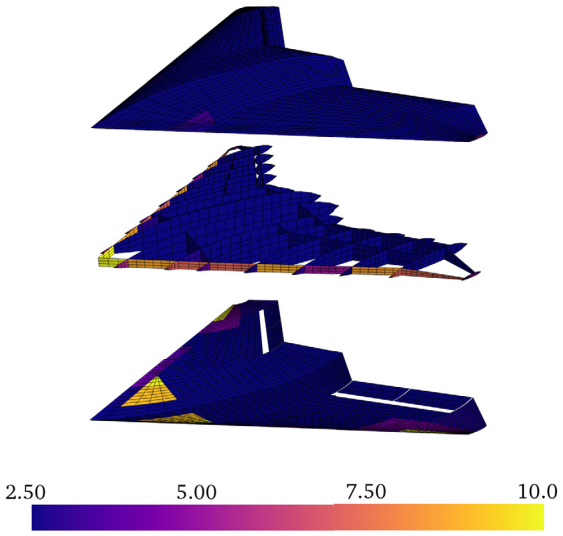

(b) Naturally stable closed loop

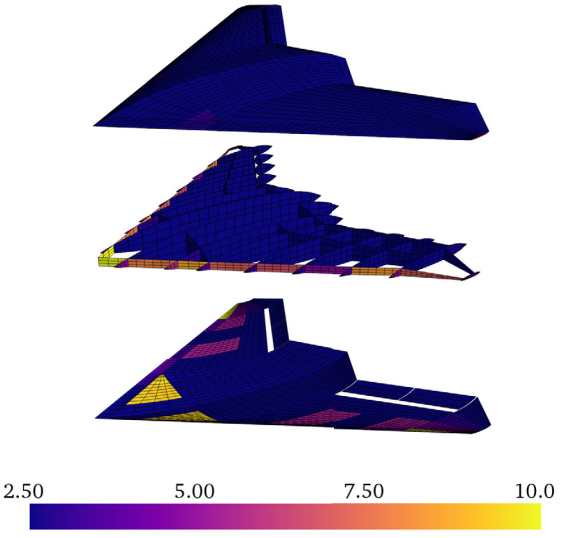

(c) Naturally unstable closed loop

Fig. 23. Resulting material thickness distribution of skin, spars and ribs in [mm].

increased successfully at the cost of moderately higher structural loads. The operation range of the aircraft is extended to unstable conditions, which could occur for mass configurations where the payload is positioned further rearwards. A re-evaluation and quantification of the resulting loads in terms of structural weight shows no significant change of the structural net weight with respect to the baseline configuration.

In general, for gust simulations the unsteady aerodynamics and the structural dynamic reactions are most important. In the case of the MULDICON, also the rigid body motion and the non-linear flight controller need to be included. It is believed that these effects are captured adequately with the presented methods. It might be interesting, but very computationally expensive, to repeat the calculations using CFD to see if that assumption holds true.

Conflict of interest statement

There is no conflict of interest.

References

[1] C.M. Liersch, K.C. Huber, Conceptual design and aerodynamic analyses of a generic UCAV configuration, in: 32nd AIAA Applied Aerodynamics Conference, American Institute of Aeronautics and Astronautics, Atlanta, GA, 2014.
[2] C.M. Liersch, K.C. Huber, A. Schütte, D. Zimper, M. Siggel, Multidisciplinary design and aerodynamic assessment of an agile and highly swept aircraft configuration, CEAS Aeronaut. J. 7 (2016) 677–694.
[3] W.R. Krüger, S. Cumnuantip, C.M. Liersch, Multidisciplinary conceptual design of a UCAV configuration, in: Proceedings AVT-MP173, North Atlantic Treaty Organization, Sofia, Bulgaria, 2011.
[4] A. Voß, T. Klimmek, Design and sizing of a parametric structural model for a UCAV configuration for loads and aeroelastic analysis, CEAS Aeronaut. J. 8 (2017) 67–77.
[5] K. Bramsiepe, A. Voß, T. Klimmek, Design and sizing of an aeroelastic composite model for an UCAV configuration with maneuver, gust and landing loads, in: Deutscher Luft- und Raumfahrtkongress, Deutsche Gesellschaft für Luft- und Raumfahrt, München, 2017.
[6] D. Schäfer, C. Vidy, C. Mack, J. Arnold, Assessment of body-freedom flutter for an unmanned aerial vehicle, in: Deutscher Luft- und Raumfahrtkongress, Deutsche Gesellschaft für Luft- und Raumfahrt, Braunschweig, 2016.
[7] A. Voß, T. Klimmek, Maneuver loads calculation with enhanced aerodynamics for a UCAV configuration, in: AIAA AVIATION Forum, American Institute of Aeronautics and Astronautics, Washington, D.C., 2016.
[8] R.M. Cummings, C.M. Liersch, A. Schütte, Multi-disciplinary design and performance assessment of effective, agile NATO air vehicles, in: AIAA AVIATION Forum, American Institute of Aeronautics and Astronautics, Atlanta, Georgia, 2018.
[9] J. Schweiger, A. Cunningham, E. Sakarya, M. Dalenbring, A. Voß, Structural design efforts for the MULDICON configuration, in: AIAA AVIATION Forum, American Institute of Aeronautics and Astronautics, Atlanta, Georgia, 2018.
[10] A. Voß, Gust loads calculation for a flying wing configuration, in: AIAA AVIATION Forum, American Institute of Aeronautics and Astronautics, Atlanta, Georgia, 2018.
[11] A. Voß, T. Klimmek, K. Bramsiepe Design, Structural optimization and loads assessment for a flying wing, in: Deutscher Luft- und Raumfahrtkongress 2018, Deutsche Gesellschaft für Luft- und Raumfahrt, Friedrichshafen, 2018.
[12] T. Klimmek, Parameterization of topology and geometry for the multidisciplinary optimization of wing structures, in: CEAS 2009 - European Air and Space Conference, Council of European Aerospace Societies, Manchester, United Kingdom, 2009.
[13] V.-F. Kunststofftechnik, Entwicklung von Bauteilen aus Faser-Kunststoff-Verbund - Berechnungen, Richtlinie VDI 2014 Blatt 3, Verein Deutscher Ingenieure, 2006.
[14] R.-G. Becker, S. Reitenbach, C. Klein, T. Otten, M. Nauroz, M. Siggel, An integrated method for propulsion system conceptual design, in: ASME Gas Turbine Technical Congress and Exposition, ASME, Montréal, Canada, 2015.
[15] M. Nauroz, Antriebskonzept einer agilen hoch gepfeilten Flugzeugkonfiguration, in: Deutscher Luft- und Raumfahrtkongress, Deutsche Gesellschaft für Luft- und Raumfahrt, Rostock, 2015.
[16] J. Katz, A. Plotkin, Low-Speed Aerodynamics: From Wing Theory to Panel Methods, McGraw-Hill Series in Aeronautical and Aerospace Engineering, McGraw-Hill, New York, 1991.
[17] E. Albano, W.P. Rodden, A doublet lattice method for calculating lift distributions on oscillation surfaces in subsonic flows, in: AIAA 6th Aerospace Sciences Meeting, American Institute of Aeronautics and Astronautics, New York, 1968.
[18] K.L. Roger, Airplane math modeling methods for active control design, in: AGARD-CP-228, NATO Advisory Group for Aerospace and Development, 1977.
[19] M. Karpel, A. Shousterman, C. Maderuelo, H. Climent, Dynamic aeroservoelastic response with nonlinear structural elements, AIAA J. 53 (2015) 3233–3239.
[20] P. Teufel, M. Kruse, Efficient method for coupling discrete gust loads analysis in the frequency domain with a fully non-linear flight control system simulation, in: IFASD, International Forum for Aeroelasticity and Structural Dynamics, Stockholm, Sweden, 2007.
[21] European Aviation Safety Agency (Ed.), Certification Specifications for Large Aeroplanes CS-25, Amendment 16, 2015.
[22] C. Buttrill, T. Zeiler, P. Arbuckle, Nonlinear simulation of a flexible aircraft in maneuvering flight, in: Flight Simulation Technologies Conference, Guidance, Navigation, and Control and Co-Located Conferences, American Institute of Aeronautics and Astronautics, 1987.
[23] M. Waszak, C. Buttrill, D. Schmidt, Modeling and Model Simplification of Aeroelastic Vehicles: an Overview, Technical Report NASA Technical Memorandum 107691, NASA Langley Research Center, 1992.
[24] M.R. Waszak, D.K. Schmidt, Flight dynamics of aeroelastic vehicles, J. Aircr. 25 (1988) 563–571.
[25] Y. Wang, A. Da Ronch, M. Ghandchi Tehrani, Adaptive feedforward control for gust-induced aeroelastic vibrations, Aerospace 5 (2018) 86.